

Chapter 4

Tunneling Spectra of Hole-Doped YBa₂Cu₃O_{6+δ}¹

4.1 Introduction

The proximity of cuprate superconductors to the Mott insulating phase gives rise to novel superconducting behavior enriched by the influence of additional orders from doping the Mott insulators [62]. Several important questions arise, concerning what characteristics these quantum orders possess, how different orders manifest themselves in various cuprates, how the competing orders relate to the superconducting order and the pseudogap phenomena, and how their presence contribute to the asymmetry of the phase diagram between the electron- (n-type) and hole-doped (p-type) cuprates. To address these issues, we study the scanning tunneling spectra of two model systems, the p-type YBa₂Cu₃O_{6+δ} and the n-type Sr_{1-x}La_xCuO₂, with the goal of contrasting the non-universal phenomena and extracting the common properties between the two types of cuprates.

The focus of this chapter is on the investigation of the hole-doped YBa₂Cu₃O_{6+δ}. While in the superconducting (SC) phase the mean-field modified BCS theory and Ginzburg-Landau theory provide a fair description for the properties of p-type cuprate superconductors; their normal-state properties seem to defy the conventional Fermi liquid phenomenology. For instance, the pseudogap (PG) phase exhibits a suppression of the density of states (DOS) around the Fermi level and a loss of spectral weight in the spin and charge excitations [9], and the anomalous metallic phase

¹The main contents of this chapter are published as N.-C. Yeh, C.-T. Chen, *et al. Phys. Rev. Lett.* **87**, 087003 (2001), and N.-C. Yeh, C.-T. Chen, *et al. Physica C* **364-365**, 450 (2001).

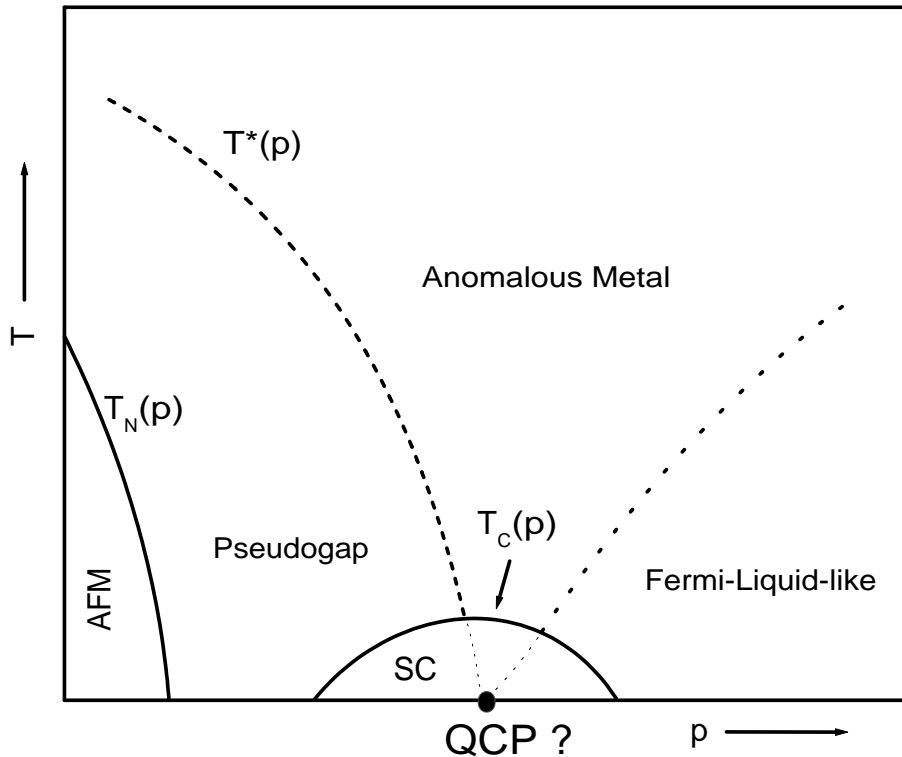


Figure 4.1: The generic temperature (T) vs. doping (p) phase diagram of the hole-doped cuprate superconductors. AFM: long-range commensurate anti-ferromagnetic order. SC stands for the superconducting state and p denotes the doping. T_N , T_c , and T^* are the Néel temperature, superconducting transition temperature, and pseudogap temperature.

exhibits the marginal Fermi liquid behavior [10] in which the single-particle and transport scattering rates are linear in frequency up to an energy comparable to the temperature [Fig. 4.1]. The linear scattering rates measured in the resistivity [165, 166] and optical conductivity [167] experiments suggest the presence of scale-invariant low-energy magnetic and density fluctuations around optimal doping above T_c . That temperature is the only energy scale dictating the fluctuation spectrum is reminiscent of the behavior of critical fluctuations associated with a quantum phase transition [168, 169]. The observation of the marginal Fermi liquid behavior [10, 74] and the PG phenomena leads to the conjecture of a quantum phase transition between the SC order and a competing order that is manifested as the PG phase, with the quantum critical point (QCP) located within the superconducting “dome” [74, 170].

Although the presence of critical fluctuations near the optimal doping level [171, 172] and the disparate physical properties between the underdoped and overdoped regimes are suggestive of the

presence of a QCP near the optimal doping, an unambiguous proof requires identifying the relevant broken symmetry associated with a critical doping p_c . Various theoretical studies have investigated the dependence of the competing ground states of doped Mott insulators on the doping level and the strength of exchange and Coulomb interactions [28, 173]. The relevant symmetries associated with the competing orders include electromagnetic $U(1)$, spin rotation-invariance $SU(2)$, square lattice space group C_{4v} , and time-reversal symmetry \mathcal{T} . Experimentally, while the $d_{x^2-y^2}$ pairing symmetry is known to dominate in the optimally doped p-type cuprates [6, 7, 174], possible doping-dependent pairing symmetry has been suggested [175]. At the time of writing, the existence of a QCP, the location of the critical doping p_c , and the nature of the quantum phase transition are still under debate.

We address some of these issues via studies of the directional and spatially resolved quasiparticle tunneling spectra on $\text{YBa}_2\text{Cu}_3\text{O}_{6+\delta}$ (YBCO) with a range of doping levels. Since YBCO has been examined extensively by various other experimental techniques and is proven less susceptible to doping-induced inhomogeneity [176] than other well-studied systems, such as $\text{La}_{2-x}\text{Sr}_x\text{CuO}_4$ (LSCO) and the highly two-dimensional (2D) $\text{Bi}_2\text{Sr}_2\text{CaCu}_2\text{O}_{8+\delta}$ (Bi-2212), its doping-dependent tunneling spectra should serve as a good reference for comparison with those of the electron-doped cuprates. By fitting to the quasiparticle momentum-dependent Blonder-Tinkham-Klapwijk (BTK) tunneling spectra of unconventional superconductors, the doping dependence of the pairing symmetry, pairing potential, and spatial homogeneity are derived. In the underdoped and optimally doped YBCO single crystals and thin-film samples, predominantly $d_{x^2-y^2}$ -wave-pairing spectral characteristics and long-range spatial homogeneity of the quasiparticle spectra are revealed. In overdoped $(\text{Y}_{0.7}\text{Ca}_{0.3})\text{Ba}_2\text{Cu}_3\text{O}_{6+\delta}$ (Ca-YBCO) thin films, however, $(d_{x^2-y^2}+s)$ pairing symmetry is found with a significant s -wave admixture. We will discuss the implication of the doping-dependent pairing symmetry on the possibility of a quantum critical point in YBCO. In addition, we will present STS data on the non-magnetic-impurity-substituted $\text{YBa}_2(\text{Cu}_{0.9934}\text{Zn}_{0.0026}\text{Mg}_{0.0004})_3\text{O}_{6.9}$ [(Zn, Mg)YBCO], where microscopic spatial modulations and strong scattering near the Zn or Mg impurity sites are observed. The results are again consistent with a $d_{x^2-y^2}$ -wave pairing as observed in the underdoped

and optimally doped pure YBCO.

4.2 Sample preparation

The samples used in this investigation include three optimally doped YBCO single crystals with $T_c = 92.9 \pm 0.5$ K, three underdoped YBCO single crystals with $T_c = 60.0 \pm 2.5$ K, one underdoped YBCO c -axis film with $T_c = 85.0 \pm 1.0$ K, two overdoped Ca-YBCO c -axis films [177] with $T_c = 78.0 \pm 2.0$ K, and one optimally doped single crystal containing small concentrations of non-magnetic impurities, (Zn,Mg)-YBCO with $T_c = 82.0 \pm 1.5$ K. All single crystals are twinned except for the (Zn,Mg)-YBCO.

The pure YBCO crystals used for the experiment are grown by a crystal-pulling technique followed by a two-week oxygen annealing. Single crystallinity with twinning is verified by x-ray diffraction. Samples for in-plane $\{100\}$ and $\{110\}$ tunneling experiments are prepared in the following manner to have their surface normal vectors align along these two directions. First, the originally c -axis oriented single crystal samples are cast in transparent epoxy holders and aligned by identifying the twinning boundary with a polarized optical microscope. Surfaces with desirable crystalline orientations are then exposed using a diamond blade and polished to optical smoothness before re-annealing. The post-annealing condition for optimal doping is 450°C in ultra-pure oxygen gas for 24 hours followed by gradual cooling. To reduce the doping of YBCO to $\delta \approx 0.5$, samples are post-annealed at 550°C in flowing argon for 72 hours and quenched to room temperatures.

Before loading onto the STM probe, the sample surface is prepared by chemical etching with 1% bromine in absolute ethanol for one minute followed by ethanol rinsing [178, 179], and kept either in high-purity helium gas or under high vacuum. Our surface preparation has the advantage of terminating the YBCO top surface at the CuO_2 plane by chemically passivating the surface layer while retaining the bulk properties of the constituent elements [178, 179]. Thus it yields reproducible spectra for samples of the same bulk stoichiometry, although direct constant-current mode atomic imaging of the chemically inert surface becomes difficult. On the contrary, surface of vacuum-cleaved YBCO samples is found to terminate at the CuO-chain layer, which is prone to loss

of oxygen and the development of surface states [178, 179, 180, 37] that plague the STS and the angle-resolved photoemission spectroscopy (ARPES) experiments [181, 182, 180, 37]. In comparison, the surface of vacuum-cleaved Bi-2212 crystals typically terminates at the BiO layer, which protects the underlying CuO_2 from loss of oxygen. Therefore, reproducible tunneling spectra representative of the bulk properties are routinely obtained on cleaved Bi-2212 surfaces [183, 54].

4.3 Results of directional tunneling spectroscopy

The spectra of YBCO single crystals are taken primarily with the normal vector of the tunneling junction (and hence the average quasiparticle momentum) along three axes: the anti-nodal axes $\{100\}$ or $\{010\}$, the nodal axis $\{110\}$, and the c -axis $\{001\}$, and those of the pure and Ca-YBCO films are taken along the c -axis. All data sets are acquired at $T = 4.2$ K with a solenoid-driven cryogenic scanning tunneling microscope and a mechanically sheared Pt/Ir tip.

4.3.1 Doping dependence of the pairing symmetry and pairing potential

Fig. 4.2 illustrates representative tunneling conductance (dI_{NS}/dV) versus voltage (V) raw data with high spatial resolution for YBCO samples at 4.2 K: (a) optimally doped YBCO crystal, with the average quasiparticle momentum $\vec{k} \parallel \{110\}$ and the tip scanning along $\{001\}$; (b) underdoped YBCO crystal, with the average quasiparticle momentum $\vec{k} \parallel \{100\}$ and scanning along $\{001\}$; and (c) Ca-YBCO film with $\vec{k} \parallel \{001\}$ and scanning along $\{100\}$. Fig. 4.3 shows the (dI_{NS}/dV) versus V spectra normalized to the high-voltage background: (a) underdoped YBCO crystal (upper panel) and (Zn,Mg)-doped YBCO crystal (lower panel) for $\vec{k} \parallel \{100\}$ together with BTK fitting curves (dashed lines); and (b) underdoped c -axis thin film (upper panel) and Ca-doped YBCO c -axis thin film (lower panel). Each set of the data is normalized relative to the polynomial fit to the high-voltage background conductance, as shown in Fig. 4.2(b) and (c) by the dashed curve.

For the optimally doped and underdoped YBCO, the STS exhibits long-range (~ 100 nm) spatial homogeneity and strong directionality, showing a zero-bias conductance peak (ZBCP) for $\vec{k} \parallel \{110\}$ [Fig. 4.2(a)], nearly “U-shape” gap features around the zero bias for $\vec{k} \parallel \{100\}$ [Fig. 4.2(b),

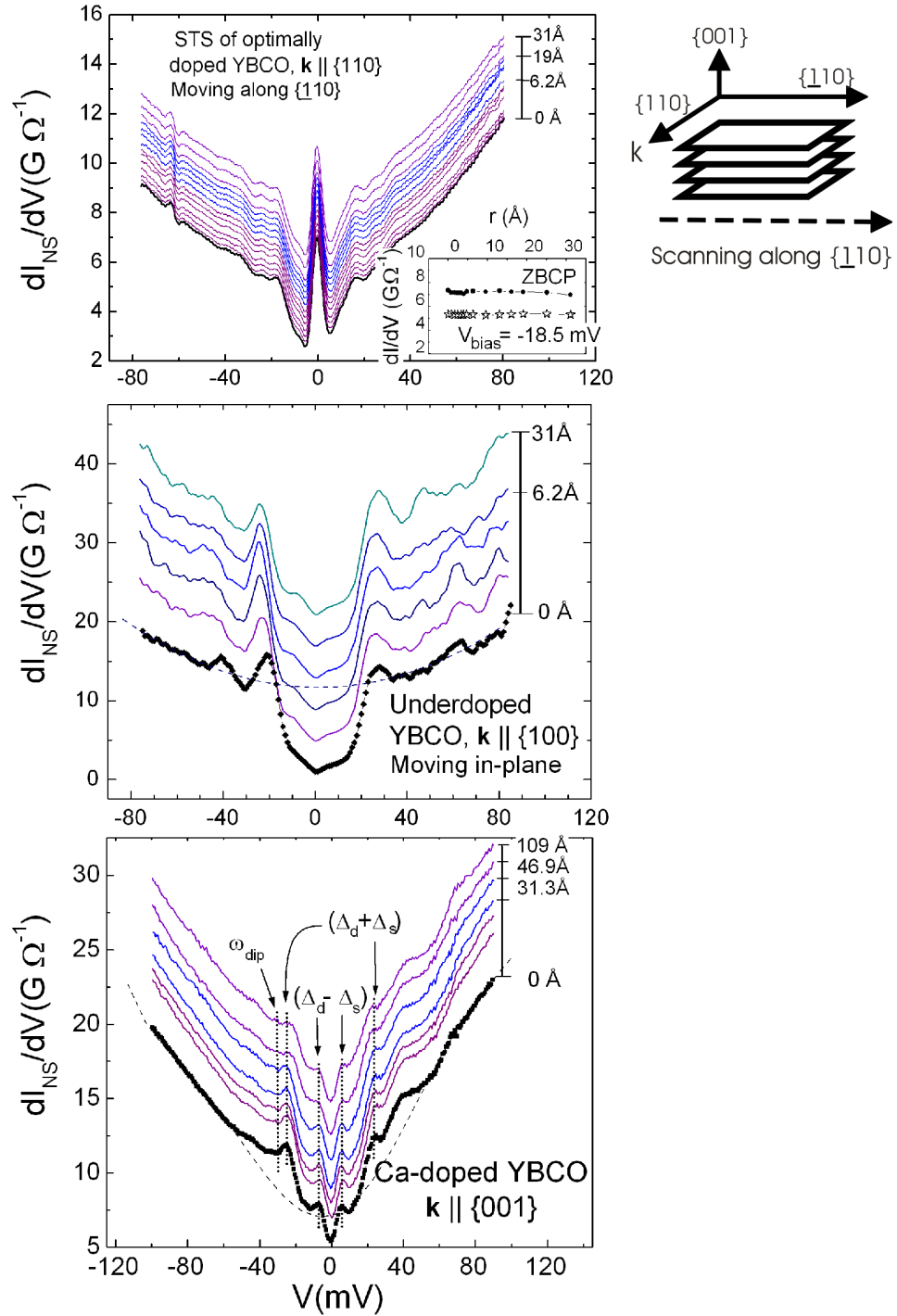


Figure 4.2: Spatially resolved (dI_{NS}/dV) vs. V spectra at 4.2 K: (a) Optimally doped YBCO crystal ($T_c = 92.0 \pm 0.5$ K) with the average quasiparticle momentum $\vec{k} \parallel \{110\}$. (b) Underdoped YBCO crystal ($T_c = 60.0 \pm 2.5$ K) with $\vec{k} \parallel \{100\}$. (c) c-axis Ca-YBCO film ($T_c = 78.0 \pm 2.0$ K). The dashed curves in (b) and (c) are the polynomial fit to the high-voltage background conductance.

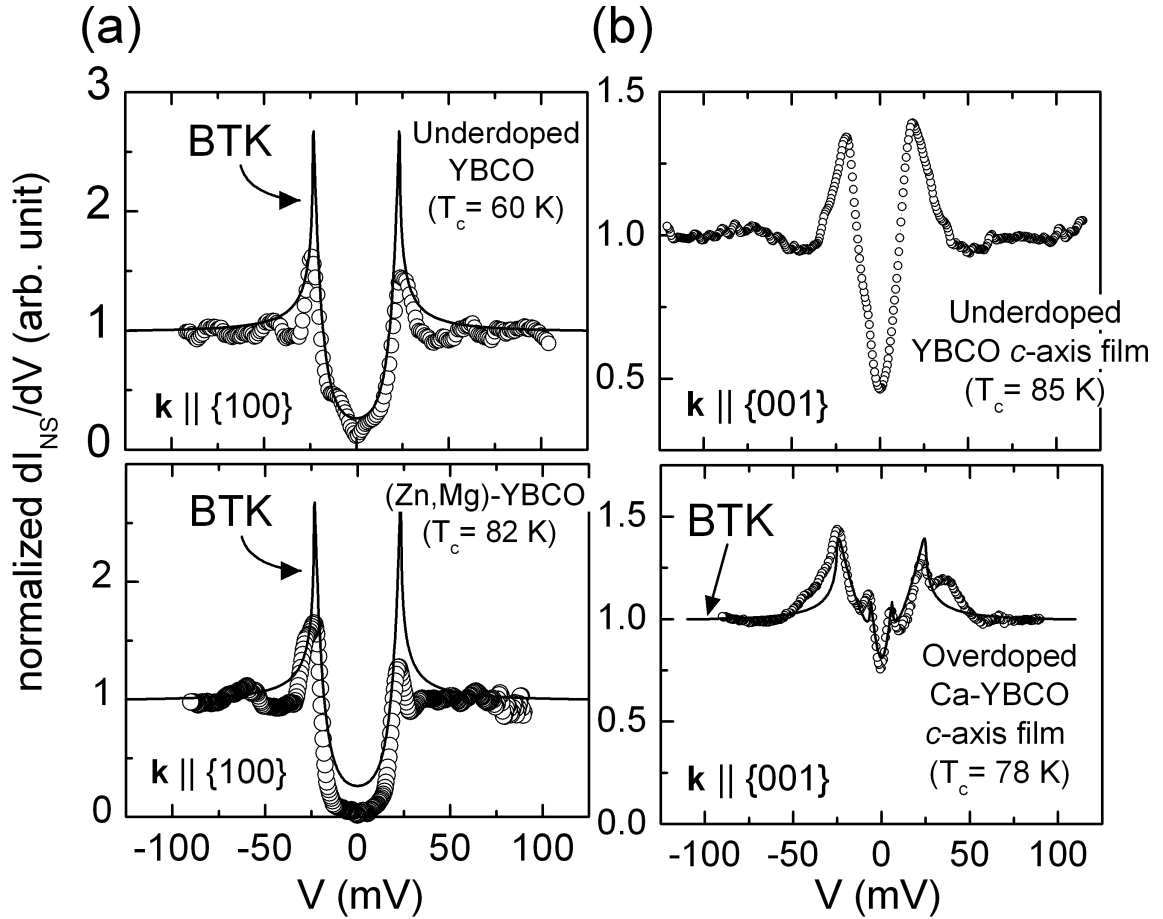
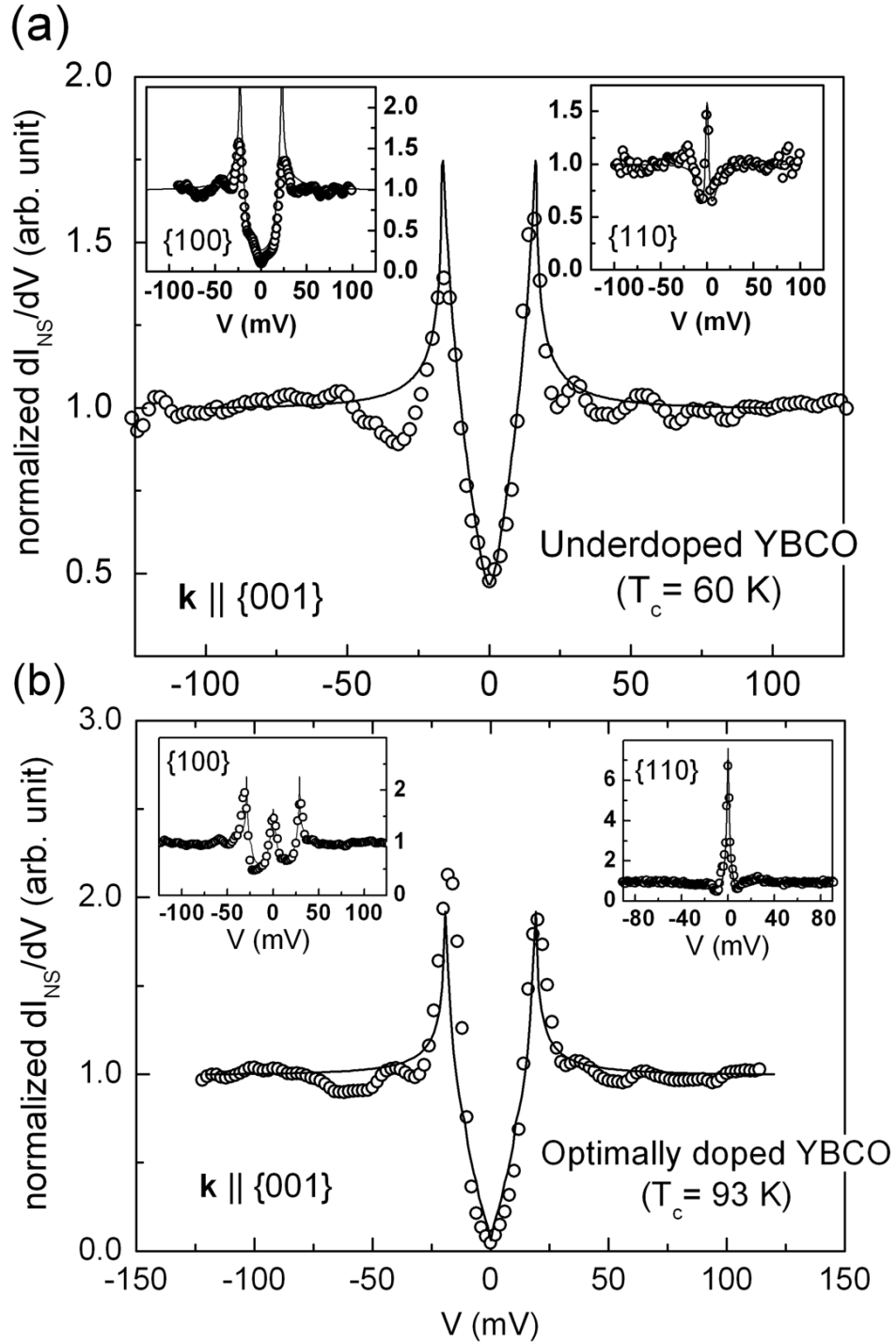


Figure 4.3: (a) Normalized $\{100\}$ spectra of an underdoped YBCO crystal with $T_c = 60.0 \pm 2.5$ K (upper panel) and that of a (Zn,Mg)-YBCO crystal with $T_c = 82.0 \pm 1.5$ K (lower panel) at 4.2 K together with a BTK fitting curve (solid line). (b) Normalized (dI_{NS}/dV) vs. V tunneling spectra of a c -axis underdoped film with $T_c = 85.0 \pm 1.0$ K (upper panel) and that of a Ca-YBCO film with $T_c = 78.0 \pm 2.0$ K (lower-panel) at 4.2K. For the BTK analysis, each data set is normalized relative to the polynomial fit to the high-voltage background conductance, as shown in Fig. 4.2 by the dashed curve. The tunneling cone [174, 184] of all data sets ranges from $(\pi/12)$ to $(\pi/8)$.



Adapted from Wei *et al.*, PRL **81**, 2542 (1998)

Figure 4.4: (a) Normalized tunneling spectra of underdoped YBCO single crystal ($T_c = 60.0 \pm 2.5$ K) with BTK fitting curves. Main panel: c -axis tunneling spectrum. Top left inset: Tunneling spectrum with averaged quasiparticle momentum \vec{k} along the anti-nodal direction. Top right inset: Spectrum taken with \vec{k} along the nodal direction. (b) Adapted from Wei *et al.* [174]. Normalized tunneling spectra of optimally doped YBCO single crystal with BTK fitting curves. We note that the $\{100\}$ spectrum shows a ZBCP feature superposed on a U-shape gap because of surface microfaceting. The data points are plotted as open circle and the BTK fitting curves as solid line.

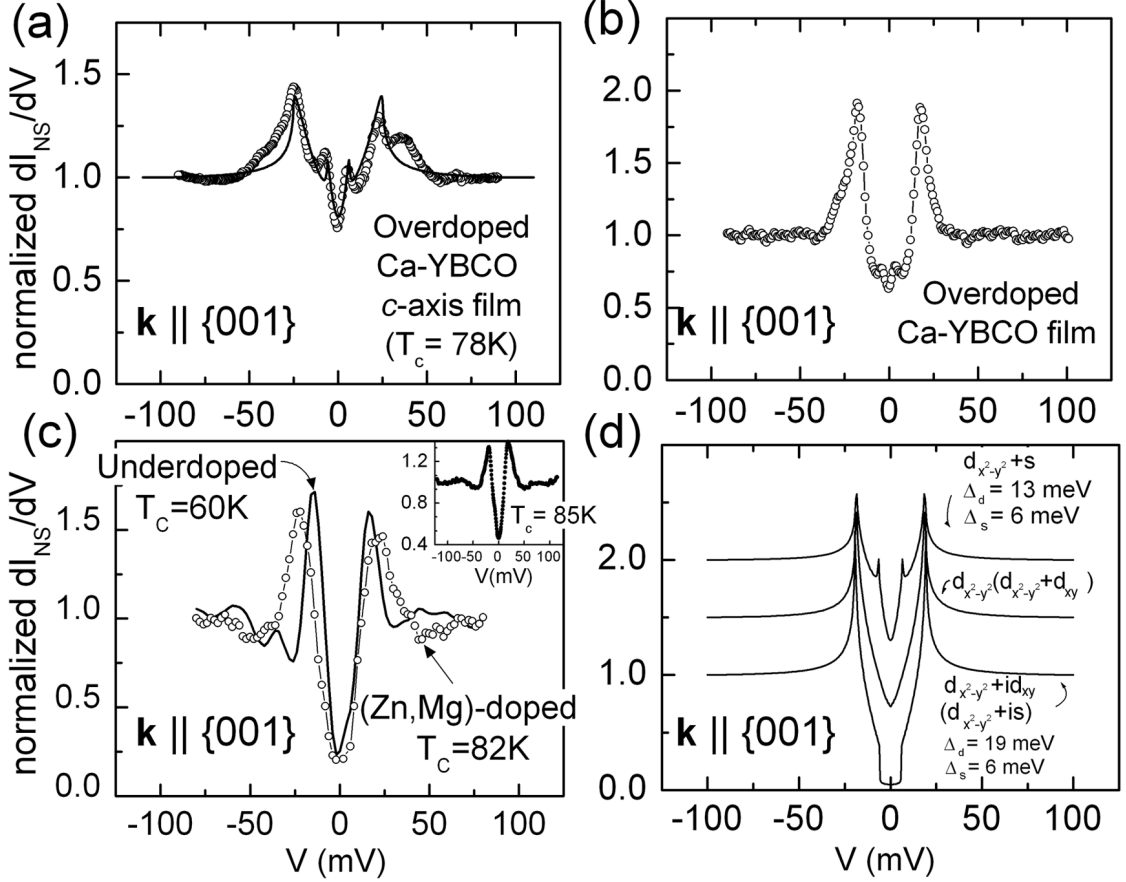


Figure 4.5: Representative c -axis tunneling spectra of YBCO. (a) Spectrum of Ca-YBCO films with $\Delta_d = 17$ meV and $\Delta_s = 9$ meV obtained by the BTK fitting (the thick solid line) to a $(d_{x^2-y^2} + s)$ -wave pairing. (b) Spectrum of YBCO films with $\Delta_d = 13$ meV and $\Delta_s = 6$ meV. (c) Normalized c -axis tunneling spectra of underdoped YBCO single crystal ($T_c = 60.0 \pm 2.5$ K) and (Zn,Mg)-YBCO ($T_c = 82.0 \pm 1.5$ K). Inset: Underdoped YBCO c -axis film ($T_c = 85.0 \pm 1.0$ K) (d) Calculated c -axis tunneling spectra for different pairing symmetries.

Fig. 4.3(a)], and “V-shape” features for $\vec{k} \parallel \{001\}$ [Fig. 4.3(b)]. By taking into account the finite transverse momentum distribution of the incident quasiparticles relative to the normal direction of the sample surface (i.e., by factoring in a finite “tunneling cone,” which typically ranges from 15° to 22.5° [174]), the prima features and the directionality of the spectra of all optimally doped and underdoped YBCO samples are consistent with d -wave pairing within the generalized BTK formalism [*cf.* §2.2] [124, 125, 123]. In Fig. 4.4, the normalized tunneling spectra of underdoped YBCO single crystal ($T_c = 60.0 \pm 2.5$ K) with BTK fitting curves are shown in comparison with the spectra of the optimally doped YBCO single crystal published by Wei *et al.* [174]. The pairing potential of the optimally doped YBCO is $25.0 - 29.0$ meV, while that of the underdoped YBCO is

22.0 – 24.0 meV.

We note that when tunneling along the $\{100\}$ or $\{010\}$ anti-nodal direction, the theoretical BTK simulation predicts a perfect U-shape with sharp coherence peaks. In real underdoped samples, however, the coherence peaks are suppressed, and disorder-induced quasiparticle states with microscopic spatial variation can exist inside the U-shape gap [Fig. 4.2(b), Fig. 4.3(a)]. The resulting V-shape residual spectra suggest that gapless nodal quasiparticles are responsible for these subgap low-energy excitations.

For the Ca-doped YBCO epitaxial films, macroscopic spatial variation in the STS at a length scale of ~ 50 nm is observed, which correlates with the dimension of the growth islands according to images of atomic force microscopy [177], while the STS's within each island are spatially homogeneous, as exemplified by Fig. 4.2(c). Furthermore, the STS of Ca-YBCO exhibits *long-range symmetric subgap peaks*, which differ from the spectral contributions of local impurities or oxygen vacancies; the latter generally appear as asymmetric and short-range humps in the spectra. These spectral features are in good agreement with $(d_{x^2-y^2} + s)$ -pairing according to the generalized BTK analysis [124, 125], with a pairing potential $\Delta_k = \Delta_d \cos(2\theta_k) + \Delta_s$, where θ_k is the angle of \vec{k} relative to $\{100\}$. Two typical sets of spectra are obtained, one with $\Delta_d = 17$ meV and $\Delta_s = 9$ meV as illustrated in Fig. 4.5(a), and the other with $\Delta_d = 13$ meV and $\Delta_s = 6$ meV in Fig. 4.2(b).²

In comparison, long-range homogeneous spectra consistent with $d_{x^2-y^2}$ -wave pairing are confirmed on the optimally doped and underdoped c -axis epitaxial films, as exemplified in Fig. 4.3(b). The c -axis tunneling spectra of the underdoped YBCO single crystal, (Zn,Mg)-doped YBCO single crystal, and those of the underdoped YBCO film are also included in Fig. 4.5(c). For clarity, we depict the calculated c -axis tunneling spectra of different pairing symmetries in Fig. 4.5(d). Under the premise that the tunneling spectra are spatially homogeneous well beyond the coherence length and mean free path, we suggest that the long-range and symmetric subgap peaks in overdoped Ca-YBCO represent supporting evidence for doping-induced variations in the pairing symmetry from predominantly $d_{x^2-y^2}$ -wave to mixed $(d_{x^2-y^2} + s)$ -wave with a substantial s -component ($\geq 30\%$).

²We suspect that the dopant distribution of the heavily overdoped Ca-YBCO thin film may have phase segregation, which can account for the various gap values observed in this sample.

4.3.2 Impurity effect

Contrary to the long-range spatial homogeneity in the quasiparticle spectra of YBCO and Ca-YBCO, microscopic spatial variations have been observed in the (Zn,Mg)-YBCO single crystal near the Zn and Mg sites, where the coherent quasiparticle peaks for the c -axis tunneling spectra are strongly suppressed and replaced by a single impurity scattering peak at an energy $\Omega < \Delta_d$. The impurity scattering spectra may be classified into two types. One is associated with a resonant scattering at $\Omega_1 \approx (-10 \pm 2)$ meV and the other at $\Omega_2 \approx (4 \pm 2)$ meV, as shown in Fig. 4.6(a).

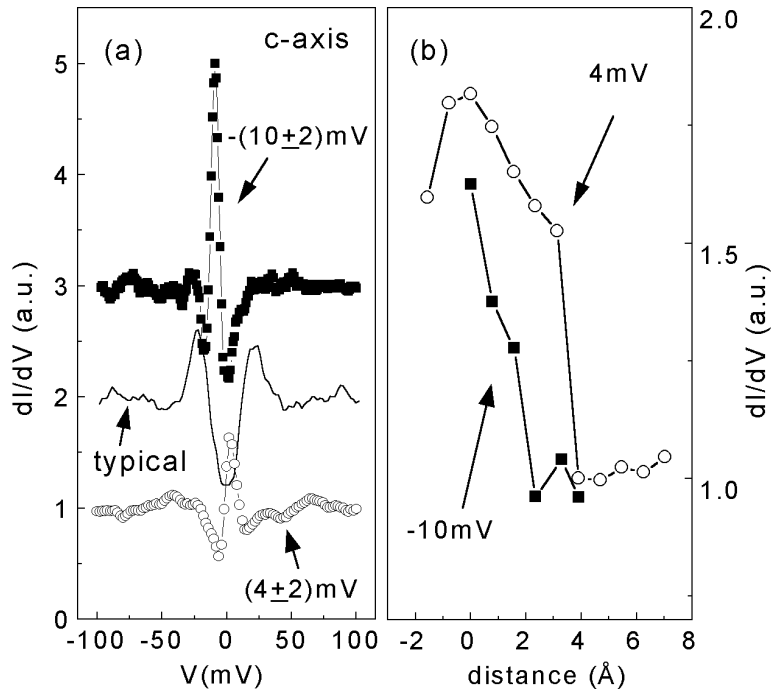


Figure 4.6: (a) Normalized c -axis tunneling spectra of the (Zn,Mg)-YBCO single crystal at and away from a local non-magnetic impurities. Two types of resonant energies are found at $\Omega \approx (-10 \pm 2)$ meV and $\Omega \approx (4 \pm 2)$ meV, corresponding to two different substitutions of Zn and Mg in the Cu – O planes. (b) Rapid decrease of the intensity of the resonant scattering peaks for displacement along $\{010\}$ away from an impurity site. The typical spectrum is recovered at ~ 3 nm away from the impurity site.

Assuming the position where the maximum intensity of a resonant peak occurs as an impurity site, we find that the peak persists over several lattice constants for displacement along either $\{100\}$ or $\{010\}$, the Cu – O bonding direction, and the peak intensity decreases rapidly within the Fermi wavelength, as shown in Fig. 4.6(b). For displacement along other directions, the spectral features become much more complicated. For example, the resonant scattering peak could appear to alternate

between energies of the same magnitude and opposite signs as the STM tip scans away from the local impurity [Fig. 4.7]. For STM tips significantly far away from any impurities, the usual c -axis quasiparticle tunneling spectrum is recovered, but the global superconducting gap Δ_d is suppressed to (22 ± 4) meV from $\Delta_d = (27 \pm 2)$ meV in pure YBCO.

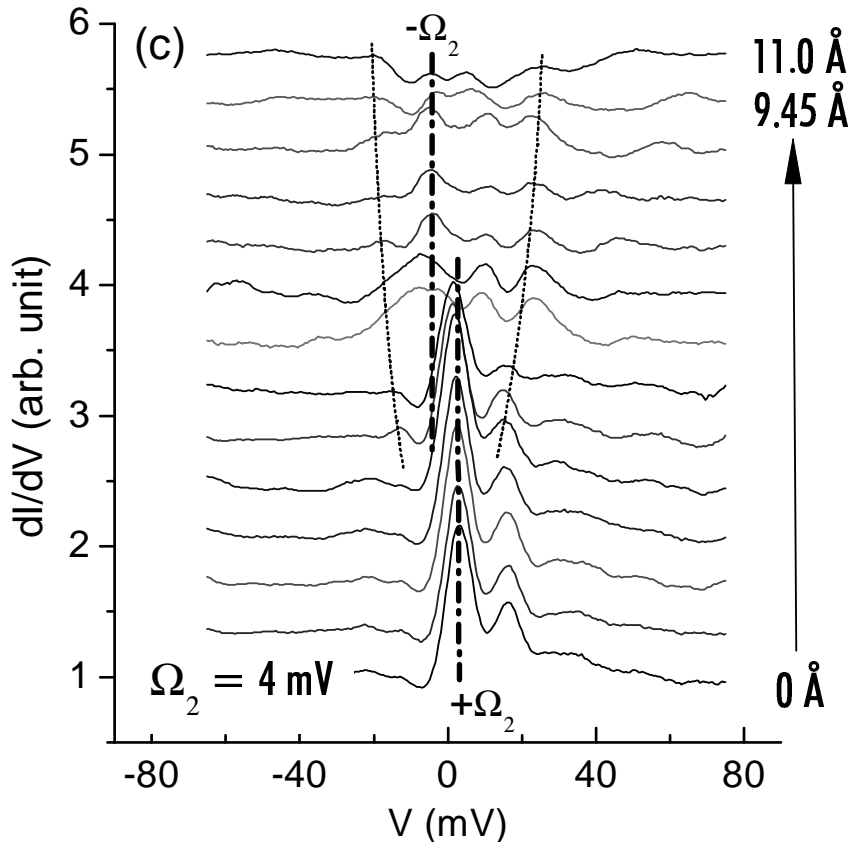


Figure 4.7: Spatial evolution of the c -axis tunneling spectra near a non-magnetic impurity with a scattering peak at $\Omega \approx +4$ meV.

4.4 Discussion

4.4.1 Pairing symmetry

It is shown in §2.2 by the generalized BTK formalism that, for superconductors with a small secondary pairing component, tunneling spectra along certain special axes can reveal the presence of the small admixture. For example, a small time-reversal-symmetry-breaking (TRSB) component,

such as is - or id_{xy} -admixture, would split the ZBCP when tunneling into the nodal direction of a predominantly d -wave superconductor [Fig. 4.8]. It would also change the gapless V-shape c -axis tunneling spectrum into a fully gapped U-shape spectrum around the Fermi level [Fig. 4.5(d)]. In comparison, the effect of an s -wave admixture in a predominantly d -wave superconductor, which breaks C_{4v} , can be manifested in the c -axis tunneling spectrum as two symmetric subgap peaks, while the spectral V-shape around the zero bias is retained [Fig. 4.5(b)].

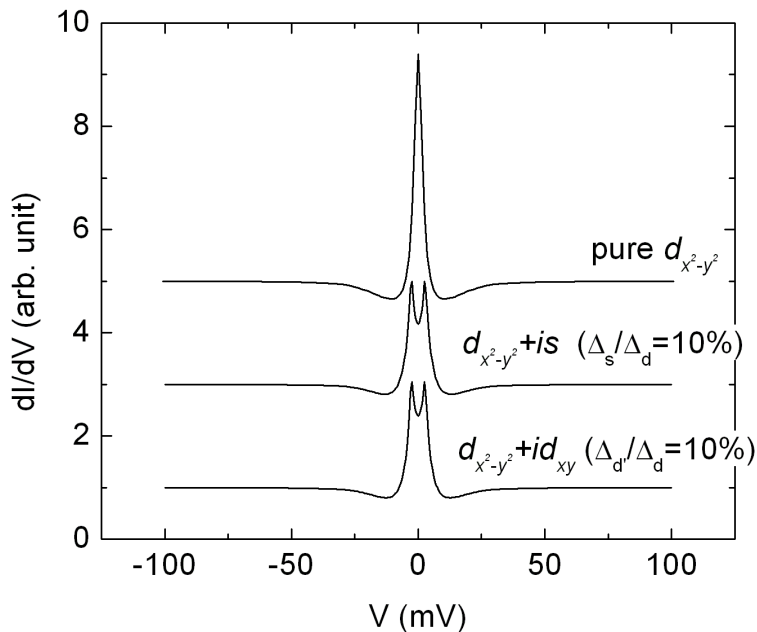


Figure 4.8: Numerical simulation of the tunneling spectra taken along $\{110\}$ for different pairing symmetries.

For convenience, the simulated $\{110\}$ spectrum for different pairing symmetries is reproduced in Fig. 4.8 as a reference. Comparing Fig. 4.8 and Fig. 4.5(d) with the experimental tunneling spectra [Fig. 4.2–4.5], we conclude that there is no TRSB component detected in either $\{110\}$ or c -axis tunneling within the STS resolution. In contrast, a significant amount of s -component ($\geq 30\%$) is revealed in the tunneling spectrum of overdoped Ca-YBCO samples.

Further experimental evidence of a mixed ($d + s$)-pairing in the overdoped YBCO family is provided by the ARPES of the fully oxygenated (lightly overdoped) YBCO single crystal [37] and the Raman spectroscopy of the heavily overdoped Ca-YBCO single crystal [38]. In addition, a sizable s -wave admixture in the SC order parameter of overdoped cuprates with tetragonal crystalline

structures, such as $\text{Bi}_2\text{Sr}_2\text{CaCu}_2\text{O}_{8+\delta}$ (Bi-2212) [38] and $\text{Tl}_2\text{Ba}_2\text{CuO}_{6+\delta}$ (Tl-2201) [185, 39], is also detected in Raman scattering experiments.

In the context of quantum criticality, our data of doping-dependent pairing symmetry is suggestive of a QCP with broken C_{4v} symmetry. However, a small s -pairing component beyond the resolution of our STS exists in the under- and optimally doped YBCO due to crystalline orthorhombicity, as identified to be $\leq 9\%$ by the recent scanning SQUID magnetometry measurement of the half-flux quantum effect [7] in YBCO/Au/Nb ramp-edge junction rings [186]. This result would imply that no obvious broken symmetry have taken place in YBCO when crossing over to the overdoped region. In contrast, the s -wave component found by Raman experiments on heavily overdoped tetragonal Bi-2212 and Tl-2201 crystals indicates that, in these two systems, there *is* a broken C_{4v} symmetry upon overdoping, thereby proving that s -wave mixing in the heavily overdoped limit is a generic feature, irrespective of sample crystalline symmetry. Although there is no obvious change of symmetry observed in YBCO with increasing hole-doping, the significant increase of s -component admixture in overdoped YBCO is indicative of an abrupt change in the ground state electronic properties with doping.

We remark that there have been suggestions of a possible QCP associated with broken time-reversal symmetry in the overdoped limit observed by macroscopic measurements including planar junctions and point-contact spectroscopy [175]. However, as mentioned above, our tunneling results are inconsistent with the existence of a secondary complex pairing component. In addition, other experimental techniques, such as the scanning SQUID magnetometry on three families of hole-doped cuprates including Ca-YBCO [187], yield no trace of the TRSB component in overdoped p-type cuprates. We note that the absence of either $(d_{x^2-y^2} + id_{xy})$ or $(d_{x^2-y^2} + is)$ in the tunneling spectra does not rule out the possibility of certain broken time-reversal-symmetry states, such as the staggered flux state [188, 189, 190] and the circulating current phase [74], for they cannot be detected directly by tunneling. To date, the only few experimental results supportive of a long-range staggered flux order (also referred to as a d -density wave order) [93, 94] or a circulating current phase [191] in the *underdoped* cuprates have been highly controversial. The latest neutron

scattering experiment on highly-ordered underdoped YBCO single crystal [87] contradicts the earlier result [93] and points to a short-range, dynamic spin density wave coexisting with SC instead of a long-range static d -density wave order.

Whether TRSB long-range order exists in the *underdoped* cuprates remains to be elucidated with future research efforts. However, it is fair to conclude that, in the *overdoped* limit, there is no experimental technique sensitive to bulk properties reporting its existence, alluding to an extrinsic origin of the complex pairing symmetry observed in certain surface sensitive tunneling experiments [175]. That is, surface degradation and faceting resulted from typical preparation of macroscopic tunneling junctions maybe responsible for the illusive and often non-reproducible TRSB components. On the other hand, an s -wave component that preserves the time-reversal symmetry while breaking the crystalline symmetry is revealed in various tunneling and bulk experiments. These observations strongly suggest a fundamental change of the ground state properties with doping. Combined with other bulk experimental results of underdoped YBCO single crystals, our tunneling spectra imply a transition from a coexisting phase of a predominantly d -wave SC order with a fluctuating competing order in the underdoped regime to a pure SC order with a sizable s -wave admixture in the heavily overdoped limit of YBCO. Consequently, while there is no obvious broken symmetry, a substantial increase of an s -wave component is observed in the tunneling spectra, which is consistent with the better charge screening, weaker on-site Coulomb repulsion, and more conventional normal-state behavior exhibited in the overdoped p-type cuprates [Fig. 4.1].

4.4.2 Spatial spectral homogeneity, pseudogap, and competing orders

In sharp contrast to the long-range homogeneous pairing potential manifested in the YBCO tunneling spectra [Fig.4.2] and the absence of inhomogeneous linewidth broadening in NMR studies [192, 193], the tunneling spectra of Bi-2212 exhibit nano-scale variations in the underdoped and optimally doped tunneling spectra [67, 68],

A simple comparison of the anisotropy ratio ξ_{ab}/ξ_c (ξ_{ab} : in-plane superconducting coherence length; ξ_c : c -axis superconducting coherence length) of YBCO ($\xi_{ab}/\xi_c \sim 5$) with that of Bi-2212

($\xi_{ab}/\xi_c > 150$) clearly indicates that YBCO has a much stronger three-dimensional electronic coupling. Furthermore, the ratio of the c -axis coherence length to the c -axis lattice constant of Bi-2212 is smaller than 0.01 while that of YBCO ranges from 0.2 – 0.7, indicating that Bi-2212 is indeed highly two dimensional (2D). According to the Hohenberg-Mermin-Wagner theorem, in a 2D system any small disturbance can disrupt the superconducting (SC) long-range order. In particular, if there is a second phase close in energy to the SC phase, it can be locally stabilized by disorder, yielding a tunneling spectrum characteristic of that competing phase and thus resulting in nano-scale spectral variations.

Recent STS measurements on Bi-2212 single crystals confirmed that the nano-scale spectra variations are related to dopant-induced disorder in this system [194]. The perturbation caused by the oxygen dopants is strong enough to locally suppress the superconducting coherence peaks and give rise to a PG-like spectrum at low temperatures. Taking into account the interlayer tunneling spectroscopy (ITS) result [150, 69, 195], which states that the PG and the sharp SC coherence peaks coexist below T_c and, above T_c , the former persists while the latter disappear, it strongly suggests that the PG observed in the ITS (and other large-area tunneling spectroscopy) experiments is dominated by the PG-like spectra near the oxygen dopants observed in STS and that it is indicative of a fluctuating competing order pinned down by disorder in Bi-2212. We will present in Chapter 6 the theoretical modeling of phase-fluctuated d -wave superconductivity coexisting with the competing order, which yields pseudogap-like spectra as observed empirically 6.4. In contrast, because of the much stronger interlayer coupling in YBCO, the SC order is more robust against disorder-induced fluctuations. Therefore, the tunneling spectrum and the bulk electronic properties show long-range homogeneity in this system.

The stabilization of a fluctuating order in Bi-2212 by oxygen disorder also explains the disparate doping dependence of the quasiparticle spectral gap of the two systems. In YBCO, the maximum value of the d -wave gap Δ_d is non-monotonic with the doping level p [Fig. 4.9(a)], whereas the ratio ($2\Delta_d/k_B T_c$) increases with decreasing doping, from ~ 7.8 for $p \approx 0.09$ to ~ 4.5 for $p \approx 0.22$, as illustrated in Fig. 4.9(b). On the other hand, tunneling experiments on Bi-2212 find an average

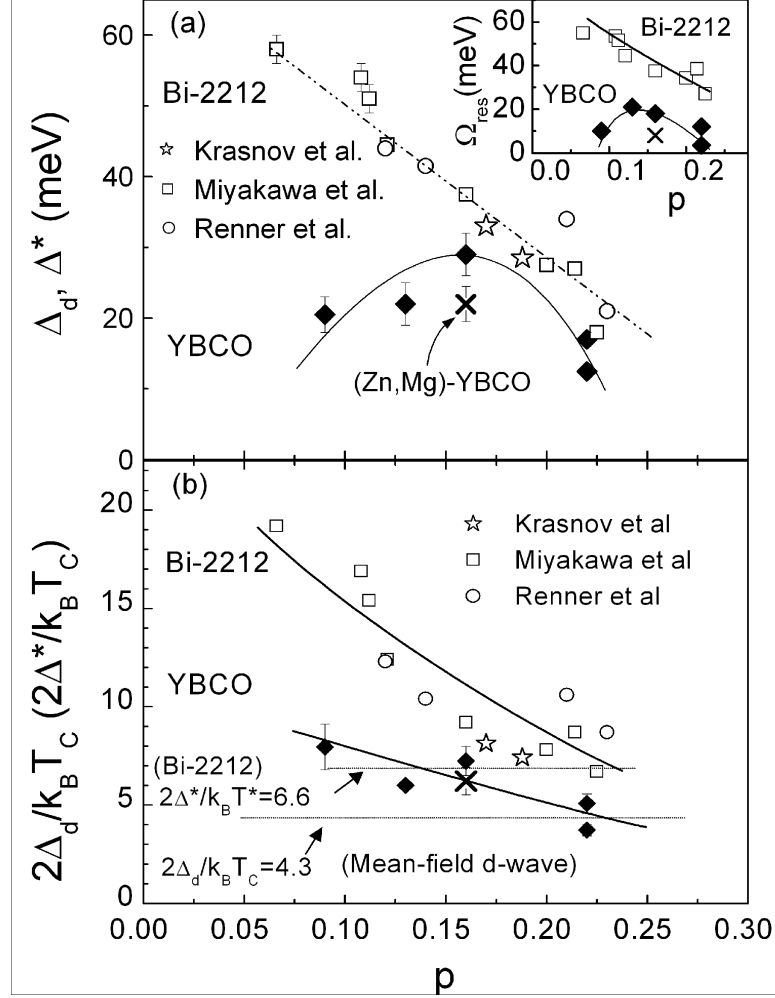


Figure 4.9: (a) Comparison of $\Delta_d(p)$ in YBCO with $\Delta^*(p)$ in Bi-2212. The doping level p is determined from the formula, $1 - T_c/T_{c,max} = 82.6(p - 0.16)^2$ [196, 197] with $T_{c,max} = 93.0$ K. Inset: Comparison of $\Omega_{res}(p)$ for YBCO and Bi-2212. (b) Doping-dependent $(2\Delta_d/k_B T_c)$ for YBCO and $(2\Delta^*/k_B T_c)$ for Bi-2212. The solid diamond denotes the YBCO data acquired in this study. The error bar associated with each doping level covers the range of Δ_d obtained from all spectra and the uncertainties of the BTK fitting. The open symbols are data extracted from three representative tunneling experiments of Bi-2212. (Open star: Krasnov *et al.* [69]. Open square: Miyakawa *et al.* [148]. Open circle: From Renner *et al.* [54]. The solid lines are guide to the eye.

gap Δ^* that increases with decreasing doping p , scales with the pseudogap temperature T^* , $2\Delta^* \sim 6.6k_B T^*$ [148, 57, 54, 198, 199, 200], and persists above T_c [9].

To understand the different trends in these two hole-doped cuprates, we examine the tunneling results on Bi-2212 in more detail. The low-temperature c -axis STM tunneling result of the optimally doped and underdoped Bi-2212 reveals two types of spectra [67, 68]. One shows sharp superconducting coherence peaks accompanied by the small satellite features located slightly above the spectral gap [67, 68] with the sharp peaks diminishing upon increasing temperatures [54]. The other type shows rounded spectral peaks [67] which resemble the PG spectra taken above T_c [54, 99]. As mentioned earlier, there is strong evidence that the nano-scale spectral variations are induced by oxygen dopants [194], and the resulting PG-like spectra are indicative of a pinned competing order coexisting with superconductivity. At the mean-field level, the spectral gap for the coexisting phase is $\Delta_{eff} \approx \sqrt{\Delta_d^2 + V_{co}^2}$, where V_{co} is the strength of the disorder-pinned competing order. As doping level decreases, because the SC pairing strength decreases, more and more regions become susceptible to disorder pinning of competing orders, which gives rise to PG-like spectra as shown in [68, 98]. Besides, the increasing strength of the competing order V_{co} starts to dominate over the diminishing Δ_d . Therefore, when the quasiparticle spectra are averaged over a macroscopic region, the average spectral gap Δ^* increases with decreasing doping, as manifested in the break-junction tunneling spectroscopy and the ARPES experiments [148, 57, 54, 198, 199, 200]. In contrast, for YBCO whose anisotropy ratio is much smaller, the superconducting order is much stiffer. Additional experiments in high fields also reveal that YBCO is farther away from quantum criticality than Bi-2212 [201, 202]. Thus, the effect of the competing phase is suppressed, and the mean-field BTK description is adequate to account for the low-energy characteristics of the tunneling spectra near and below the superconducting gap so that the measured energy gap Δ_d appears to track T_c better. In Chapter 6, we shall provide the theoretical foundation that justifies the conclusions drawn from experiments.

4.4.3 Satellite features

Although the generalized BTK analysis is suitable for deriving the pairing potential and the primary spectral characteristics, it cannot account for the satellite spectral features associated with many-body interactions [159, 203, 204]. In Bi-2212, the high-energy spectral “dip-and-hump” features [148, 57, 54, 198, 199, 200] are generally attributed to quasiparticle damping via interactions with collective bosonic excitations [159, 203, 204]. In the strong coupling limit, the spectral dip is expected to appear at the energy $\omega_{dip} = \Delta + \Omega_{res}$, where Δ is the measured gap, and Ω_{res} is associated with the resonance of the collective excitations [159, 203, 204]. If we adopt the notion that the ground state of YBCO is purely superconductivity and the bosonic excitations are responsible for the satellite features, we may define Ω_{res} as the energy difference between the primary peak (Δ) and the dip (ω_{dip}) [203], as indicated by the dotted lines in Fig. 4.2(c), and we find that Ω_{res} in YBCO decreases with decreasing p , as shown in the inset of Fig. 4.9(a).

There have been heated debates about the nature of these many-body bosonic modes [205, 206, 207]. The possible candidates of the bosonic excitations include the magnetic resonance mode [205], the B_{1g} phonon mode [208], and the longitudinal optical phonon mode [209]. They all have similar energy scales, and thus to distinguish between the three is non-trivial. According to the tunneling spectra of YBCO, the magnitude of the global Δ and Ω_{res} in (Zn,Mg)-YBCO both become smaller than those of the optimally doped YBCO, as shown in Fig. 4.9(a). The strong suppression of Ω_{res} by doping small amount of impurities with atomic masses similar to Cu but with different spin states suggests that if the satellite features arise from the bosonic modes, then it is the magnetic excitations, not phonons, that couple to the electrons and result in the “dip-and-hump” features. The latest ARPES data on Zn- and Ni-substituted Bi-2212 have demonstrated a significant reduction of the real part of the electron self-energy upon impurity substitution that disrupts the anti-ferromagnetic spin fluctuations in Bi-2212 [210], providing additional strong evidence for the magnetic origin of “dip-and-hump” features in p-type cuprates.

While in our earlier publications we had analyzed the satellite features of YBCO quasiparticle tunneling spectra in the context of bosonic excitations coupled with the quasiparticles of a pure su-

perconducting state, we notice that the energy scale of the bosonic mode deduced from the tunneling spectra is substantially smaller than that obtained directly from the bulk neutron scattering experiments. Thus, we adopt an alternative interpretation that views the ground state of the cuprates as a coexisting phase of superconductivity and a relevant competing order, so that the satellite features are in fact the manifestation of the competing order with an effective gap $\Delta_{eff} \approx \sqrt{\Delta_d^2 + V_{co}^2}$. This alternative view has the advantage of consistently accounting for the presence of pseudogap phenomena and satellite features in hole-doped cuprates versus the complete absence of both the pseudogap and satellite features in electron-doped cuprates by simply varying the relative strength of superconductivity to the competing order from hole- to electron-doped cuprate superconductors. The details of the theoretical modeling will be provided in Chapter 6.

4.4.4 Quantum impurities

In a conventional s -wave superconductor, according to Anderson's theorem [211], non-magnetic impurities (*i.e.*, spinless with $S = 0$, such as Zn^{2+} , Mg^{2+} , Li^+ and Al^{3+}) are weak pair breakers because the time-reversal symmetry is preserved. Pairing of the time-reversed degenerate states leads to the same T_c and the same BCS density of states (DOS) as that of a pure superconductor. It is the magnetic impurities that break the time-reversal symmetry, which strongly suppresses T_c and modifies the DOS [212].

In contrast, the gapless nature of the $d_{x^2-y^2}$ - or $(d_{x^2-y^2} + s)$ -pairing symmetry and the presence of gapless nodal quasiparticles in hole-doped cuprates result in their drastic response to the non-magnetic impurities. The spinless quantum impurities that substitute the Cu^{2+} ions in the CuO_2 plane incur strong suppression of superconductivity due to the resulting potential scattering of the nodal quasiparticles [213, 214]. In addition, Kondo effects are expected because of the induced magnetic moments [215, 216, 217, 218] associated with the non-magnetic impurities in the background of nearest-neighbor paired singlets. The induced magnetic moments can significantly perturb the immediate vicinity of the impurity site, yielding suppression of superconductivity below T_c and a strong effect on the spin dynamics above T_c [219].

That the non-magnetic impurities, such as Zn^{2+} and Mg^{2+} in YBCO, are strong pair breakers suppressing the coherence peaks and modifying the superconducting density of states [Fig. 4.6] is supportive of the presence of nodal quasiparticles in a pure d -wave superconductor [220, 216, 214, 213, 221, 217, 222, 223]. Furthermore, the single scattering peak at a non-magnetic impurity site is incompatible with any broken \mathcal{T} -symmetry component in the pairing potential, for the latter would result in two excitation peaks at $\pm\Omega$ [221]. Hence the absence of double peaks in the quasiparticle spectra of both YBCO [8] and Bi-2212 [183] provides additional confirmation of a gapless Fermi surface in the superconducting state of the hole-doped cuprates.

4.5 Summary

In conclusion, we have demonstrated the long-range spatial homogeneity in the tunneling spectra of YBCO samples with a number of doping levels. In contrast, the spectral characteristics of the (Zn,Mg)-YBCO exhibit microscopic variations indicating strong pairing breaking effects near the Zn and Mg impurities. The quasiparticle spectral features and the impurity scattering effects in the optimally doped and underdoped YBCO are consistent with a predominantly $d_{x^2-y^2}$ ($> 95\%$)-wave pairing, whereas those of the overdoped Ca-YBCO exhibit $d_{x^2-y^2}$ pairing with a significant s -component mixing ($\geq 30\%$), indicative of a change of ground state properties. Except for the higher-energy satellite features, all low-energy spectral characteristics are well captured by the generalized BTK theory, indicating that critical fluctuations play a minor role in determining the single-particle low-energy excitation spectra and that mean field theory provides a reasonable description for the subgap quasiparticle tunneling spectra in the superconducting state of YBCO. The notion is further corroborated by the studies of the vortex-state quantum fluctuations in various cuprate superconductors, which reveal that YBCO is further away from quantum criticality than most other families of cuprate superconductors.